catalysts

MDPI

Article

Hydrothermally Carbonized Waste Biomass as Electrocatalyst Support for α-MnO_2 in Oxygen Reduction Reaction

Harold O. Panganoron [1,2,3], Jethro Daniel A. Pascasio [1], Eugene A. Esparcia Jr. [1], Julie Anne D. del Rosario [1] and Joey D. Ocon [1,2,*]

1 Laboratory of Electrochemical Engineering, Department of Chemical Engineering, College of Engineering, University of the Philippines, Diliman, Quezon City 1101, Philippines; harold.panganoron@upd.edu.ph (H.O.P.); japascasio@up.edu.ph (J.D.A.P.); eaesparcia@upd.edu.ph (E.A.E.J.); jddelrosario2@up.edu.ph (J.A.D.d.R.)

2 Energy Engineering Program, National Graduate School of Engineering, University of the Philippines, Diliman, Quezon City 1101, Philippines

3 Samar State University–Mercedes Campus, Catbalogan City 6700, Philippines

* Correspondence: jdocon@up.edu.ph

Received: 19 December 2019; Accepted: 27 January 2020; Published: 3 February 2020

Abstract: Sluggish kinetics in oxygen reduction reaction (ORR) requires low-cost and highly durable electrocatalysts ideally produced from facile methods. In this work, we explored the conversion and utilization of waste biomass as potential carbon support for α-MnO_2 catalyst in enhancing its ORR performance. Carbon supports were derived from different waste biomass *via* hydrothermal carbonization (HTC) at different temperature and duration, followed by KOH activation and subsequent heat treatment. Scanning electron microscopy (SEM), Fourier transform infrared spectroscopy (FTIR), energy dispersive X-ray spectroscopy (EDX) and X-Ray diffraction (XRD) were used for morphological, chemical, and structural characterization, which revealed porous and amorphous carbon supports for α-MnO_2. Electrochemical studies on ORR activity suggest that carbon-supported α-MnO_2 derived from HTC of corncobs at 250 °C for 12 h (CCAC + MnO_2 250-12) gives the highest limiting current density and lowest overpotential among the synthesized carbon-supported catalysts. Moreover, CCAC + MnO_2 250-12 facilitates ORR through a 4-e^- pathway, and exhibits higher stability compared to VC + MnO_2 (Vulcan XC-72) and 20% Pt/C. The synthesis conditions preserve oxygen functional groups and form porous structures in corncobs, which resulted in a highly stable catalyst. Thus, this work provides a new and cost-effective method of deriving carbon support from biomass that can enhance the activity of α-MnO_2 towards ORR.

Keywords: hydrothermal carbonization; biomass; hydrochar; activated carbon; MnO_2/C; oxygen reduction reaction

1. Introduction

The use of electrochemical energy technologies, such as batteries and fuel cells, are effective and practical ways of dealing with stability issues brought by intermittent renewable energy sources. At present, lithium-ion chemistries dominate among energy storage technologies and cover a wide array of applications. However, metal-air batteries (MABs) are also seen to address the challenges for renewable energy applications and other niche applications [1,2].

The utilization of ambient air in energy storage applications is constrained by the sluggish kinetics of the oxygen reduction reaction (ORR) [3]. As such, previous studies have focused on the development of electrocatalysts to enhance ORR performance [4–6]. ORR electrocatalysts should provide low ORR

overpotential, high durability, and selectivity towards the ideal 4-electron (e^-) pathway. Moreover, the material should be abundantly available and can be easily synthesized [7]. Electrocatalysts that were previously investigated include precious metals and their alloys, transition metals, metal oxides, and carbon-based materials [1]. Transition metal oxides have also been formed into a matrix with carbon-based structures to improve ORR activity [8–10]. Among the transition metal oxides, manganese oxides (MnO_2) are widely recognized as suitable ORR catalysts due to their high catalytic activity, low cost, and environmental friendliness [11–13].

MnO_2 comes in various polymorphs. Two of which, α-MnO_2 and δ-MnO_2, are reported to have the relatively high ORR catalytic activities [12,13]. The former is considered to have better performance due to higher Mn^{3+} surface concentration, which allows for more electroactive sites for catalysis [14]. The drawbacks of α-MnO_2, however, include poor conductivity and low stability. Thus, catalyst supports such as carbon black, graphene, and carbon nanotubes are typically used to improve MnO_2's catalytic performance [10,15].

Catalyst supports assist in metal dispersion and morphological formation of the electrocatalyst. As a result, heat and mass transfer properties are enhanced, thereby improving catalyst efficiency [16]. Moreover, interactions of the carbon support and the metal species result in a faster electron transfer and improved absorption/desorption characteristics for oxygen intermediates [17]. Conversion of low-cost carbon-based materials to catalyst supports, however, involves complex methods [18]. Therefore, facile methods for carbon-based support synthesis are investigated in several studies [19–24].

For an efficient, low-cost production, carbon can be derived from different sources, including waste biomass [19]. Natural structures in biomass such as periodic patterns, hierarchical organization, and nanoarchitectures allow for special properties such as super hydrophobicity, structural coloration, and biological self-assembly. These structures can also provide networks for electrochemically active sites, which are beneficial for catalysis [20,21]. Mass producible biomass such as jackfruit seeds [19], eggplant [23], and silk [24] have been explored for electrocatalyst materials and showed promising results as carbon-based supports and air electrodes.

Among the different methods used to carbonize biomass, hydrothermal carbonization (HTC) is considered as the most cost-effective since it allows for the conversion of high moisture materials [25,26]. HTC requires no prior drying, utilizes water as media, and produces a lignite-like product [27]. This process is carried out at 180–250 °C under autogenous pressure. Carbon and hydrogen in the feedstock undergo decomposition by dehydration and decarboxylation [28]. The properties of the HTC product (called hydrochar) can be controlled by varying the synthesis conditions such as temperature, pH, and residence time [28–32]. Activation using potassium hydroxide (KOH) can also be employed to further enhance the porosity, surface area, and total pore volume of the hydrochar [33].

In this work, we investigate the derivation of carbon supports from different waste biomass materials including corncobs, coffee waste grounds, rice hulls, and coconut lumber sawdust. Their potential viability as carbon supports are then evaluated based on their morphology, and their ORR activity when used as support for α-MnO_2. Carbon supports were prepared *via* HTC at different temperatures and durations, followed by KOH activation. Treatment of waste biomass at 250 °C for 12 h produced carbon-supported MnO_2 with the highest ORR catalytic activity. This work provides a new and cost-effective method of deriving carbon supports from biomass through HTC for effective and durable ORR electrocatalysts.

2. Results and Discussion

2.1. Hydrothermal Carbonization

The presence of oxygen functional groups from cellulose and aromatic carbon bonds in lignin were investigated using Fourier transform infrared (FTIR) spectroscopy (Figure 1). The summary of peaks and the corresponding functional groups are summarized in Table 1.

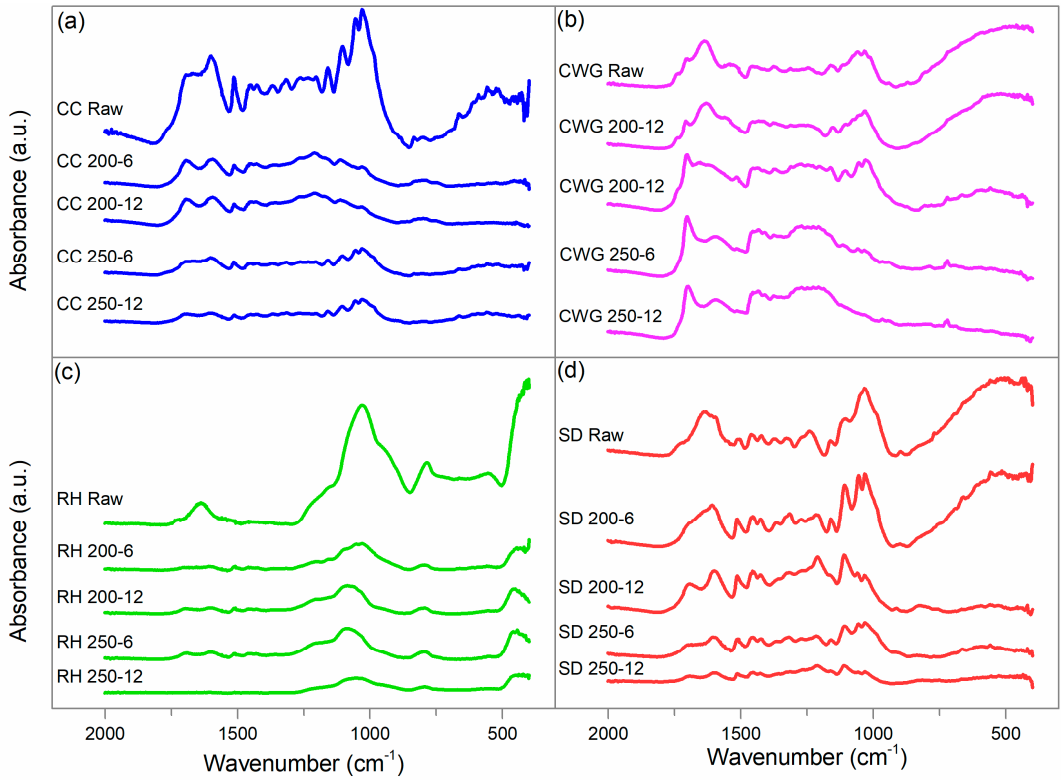

Figure 1. FTIR spectra of raw and hydrochars of (**a**) corncobs (CC), (**b**) coffee waste grounds (CWG), (**c**) rice hull (RH) and (**d**) coconut sawdust (SD) at different temperatures (200 and 250 °C) and residence time (6 and 12 h).

Table 1. Peaks and associated functional groups of produced hydrochars.

Peaks (cm^{-1})	Functional Group	Reference
1655–1700	C=O and C=C vibration from ketones and aromatic ring structures	[34]
1450–1510	C=C–C bonds vibration in an aromatic ring	[35]
1310–1410	O–H bends and aliphatic CH_3 and CH_2 deformation	[35]
1050–1270	Aryl–O and C–O stretch from ether compounds	[36]
1000–1055	C–O bonds in glucose	[36]
900	C–H groups with aromatic out-of-plane bends	[37,38]

The HTC process reduced the volatile oxygen functional groups from cellulose (1655, 1310, 1270 and 1050 cm^{-1}). The high thermal stability of lignin [39], however, resulted in the preservation of functional groups in aromatic rings (1600, 1500 and 1450 cm^{-1}). Increasing the temperature from 200 to 250 °C resulted to a higher degree of degradation compared to increasing the HTC duration from 6 to 12 h.

The changes in the morphological structures were examined using scanning electron microscopy (SEM). SEM images of raw and hydrothermally carbonized samples are shown in Figure 2. After HTC, the porous structures are preserved with lignin serving as the backbone [39]. Increasing the HTC temperature resulted in size reduction of globular masses found in the hydrochars. This is due to nucleation and polymerization reactions, which led to the breakage of the fibrous structure and the creation of micrometric cellulose fragments [40]. Similarly, an increase in the residence time resulted in the formation of a different hydrochar with polyaromatic structure, which consists of the polymerized fragments [41]. From the SEM images, rice hull (RH) was observed to have the least surface variation before and after treatment compared to the other samples. Similar observations were made for the HTC of RH in other studies, which were attributed to partial carbonization at the given HTC conditions. Therefore, the hydrochar from RH is expected to have low surface area and pore volumes [42].

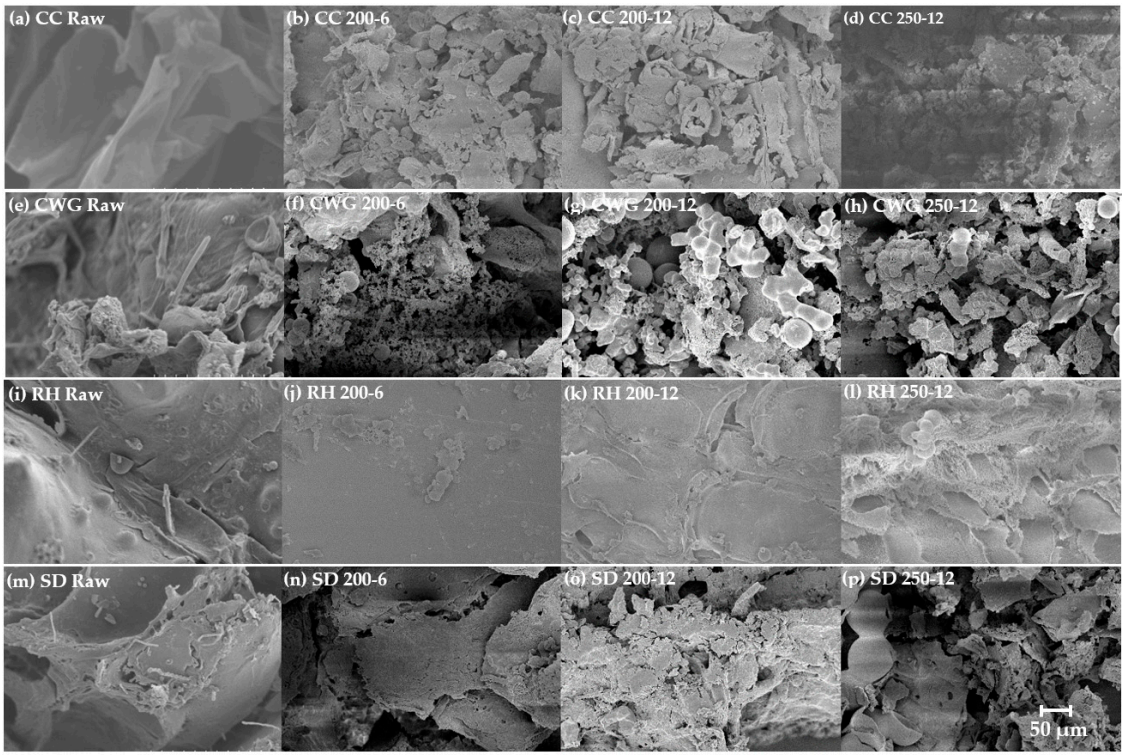

Figure 2. SEM images at 2500× magnification of the (**a–d**) corncobs (CC), (**e–h**) coffee waste grounds (CWGs), (**i–l**) rice hull (RH) and (**m–p**) coconut sawdust (SD) at varying HTC temperatures (200 and 250 °C) and duration (6 and 12 h). A measurement scale is located at the lower-right of the figure.

2.2. *Activation*

The hydrochars from the different biomass samples were then subjected to KOH activation followed by heat treatment at 600 °C in an N_2 environment. The effect of activation on the functional groups of hydrochars was then examined using FTIR, as shown in Figure 3. Results showed reduction of peak strength of the functional groups in all waste biomass samples due to volatilization and degradation [30,43]. Coffee waste grounds (CWG) and RH showed a relatively higher degree of functional group degradation compared to corncobs (CC) and coconut sawdust (SD). Among the samples subjected to HTC at 250 °C for 12 h prior to activation, activated CWG (CWGAC) and activated RH (RHAC) exhibited the lowest peaks while activated CC (CCAC) and activated SD (SDAC) retained aromatic groups at peaks located at 1655, 1310, 1270 and 1050 cm^{-1}.

The morphological examination of hydrochars after KOH activation and heat treatment are shown in Figure 4. Under the same activation conditions, samples that were pre-carbonized through HTC at 250 °C and 12 h showed higher degrees of formation of porous structures compared to those at lower temperature and residence time. Activation allowed for the opening of more pores, which were not achieved through HTC alone. Increased pore formation translates to formation of networks that can provide active sites for ORR [44]. Further, pre-carbonization reduces the formation of carbonaceous intermediate defects while it increases the micropore formation [45]. The pre-carbonization step (HTC) before activation was therefore essential in achieving stable and effective carbon support structures.

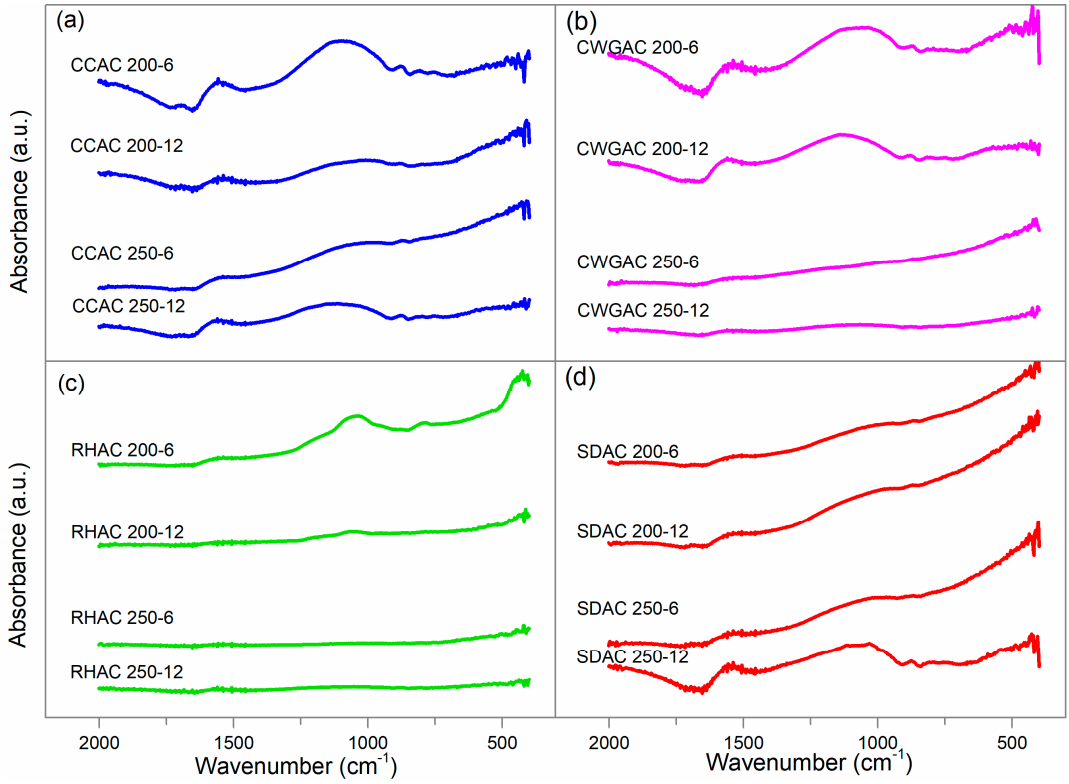

Figure 3. FTIR spectra of activated carbon from (**a**) corncobs (CCAC), (**b**) coffee waste grounds (CWGAC), (**c**) rice hull (RHAC) and (**d**) coconut sawdust (SDAC).

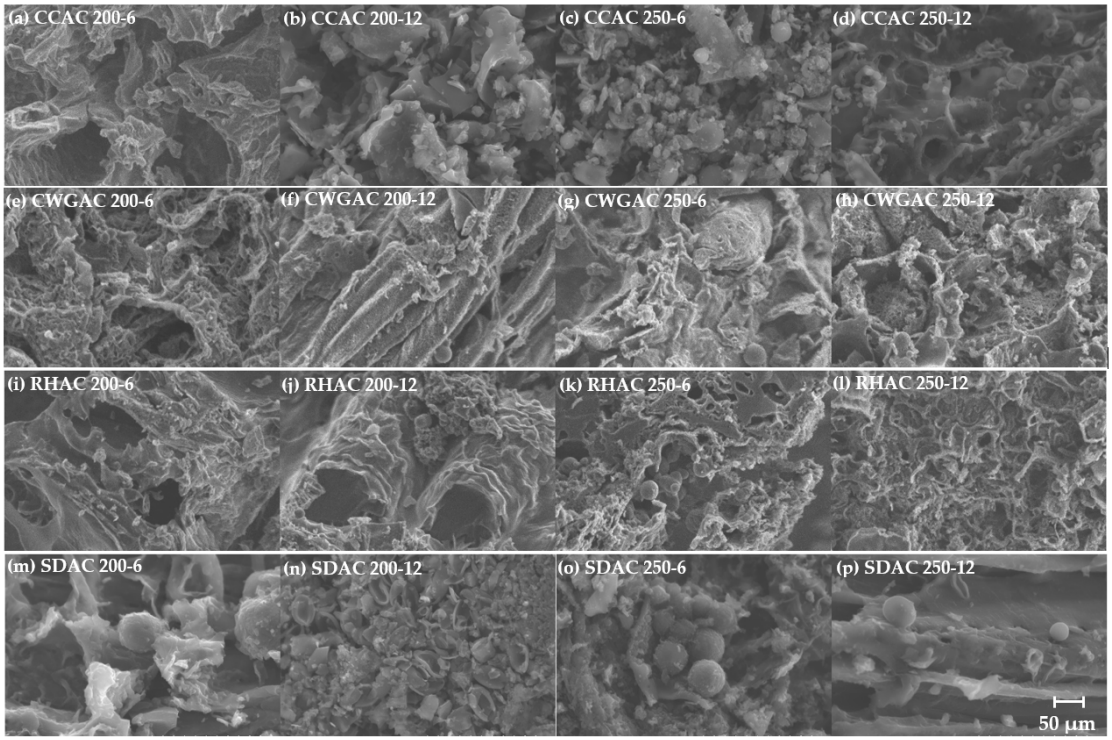

Figure 4. SEM images at 2500× magnification after activation of (**a–d**) corncobs (CCAC), (**e–h**) coffee waste grounds (CWGAC), (**i–l**) rice hull (RHAC) and (**m–p**) coconut sawdust (SDAC) that were pre-carbonized in HTC temperatures (200 and 250 °C) and residence times (6 and 12 h).

The elemental composition of the raw biomass and activated carbons that were analyzed using energy dispersive X-ray (EDX) spectroscopy are summarized in Table 2. The results show an increase in the carbon concentrations and the reduction of other elements after HTC and KOH activation. Of the samples that were synthesized, CCAC 250-12 showed the highest carbon concentration. Analysis of RHAC 250-12 showed that silicon (Si) was still present after carbonization. EDX data also indicate that there were no metals or other impurities in the synthesized carbon supports other than silicon (in the form of silica), which is inherently present in rice hulls [42]. This result also supports the FTIR results of the samples that were subjected to HTC at 250 °C for 12 h since no peaks were found at 1342–1260 cm^{-1} and 710–570 cm^{-1}. Such peaks are used to gauge the presence of C–N and C–S bonds respectively [36–38].

Table 2. Elemental composition of raw biomass and activated carbons.

Sample	%Weight Concentration					
	C	O	N	K	Si	Total
CC Raw	42.36	52.66	3.95	1.02		100.00
CCAC 250-12	83.40	16.60				100.00
CWG Raw	39.01	47.90	12.02	1.08		100.00
CWGAC 250-12	76.79	23.21				100.00
RH Raw	46.06	22.70	3.56	0.00	27.68	100.00
RHAC 250-12	61.92	31.71			6.38	100.00
SD Raw	41.33	49.38	8.41	0.89	0.00	100.00
SDAC 250-12	73.66	26.34				100.00

The crystal phase of activated carbon was determined using XRD (Figure 5). In the analysis, a broad peak was identified at 15–30 degrees, which indicates the presence of amorphous carbon [46,47]. The broad diffraction peaks in 20.8 and 21.6 in XRD pattern refers to the (002) facet [46]. Among the samples, higher intensities were observed for CCAC 250-12 and SDAC 250-12. Sharp peaks that were generated were attributed to the gold (Au) metal holder used in the XRD analysis.

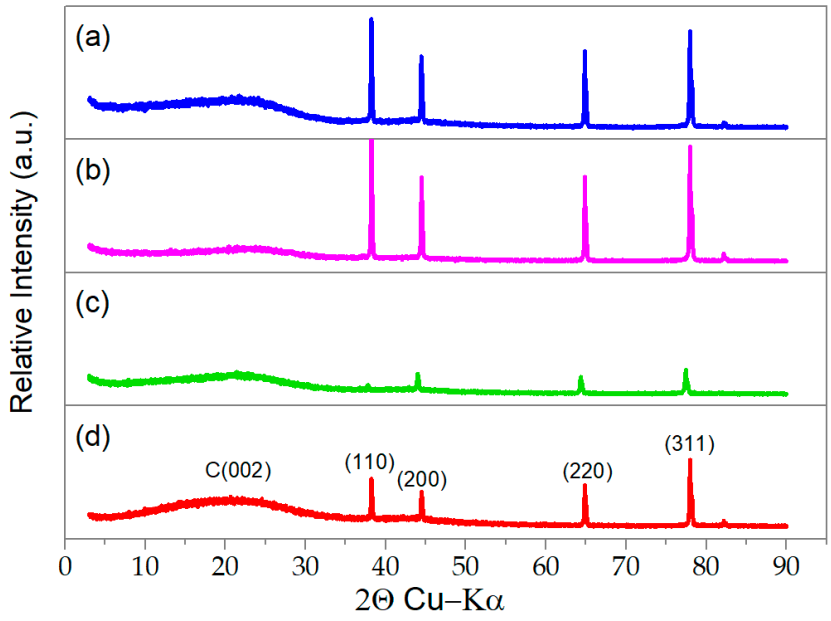

Figure 5. XRD data for (**a**) CCAC 250-12, (**b**) CWGAC 250-12, (**c**) RHAC 250-12 and (**d**) SDAC 250-12.

2.3. Incorporation of MnO_2

The hydrochars and activated carbons from the different biomass were embedded with an MnO_2 catalyst *via* the hydrothermal method. Figure 6 shows SEM images of activated samples after MnO_2 embedding. Based on the images, the change in the surface roughness of the samples indicate that MnO_2 was successfully embedded into the carbon supports. In Figure 7, the presence of the α-MnO_2 was confirmed by the XRD peaks.

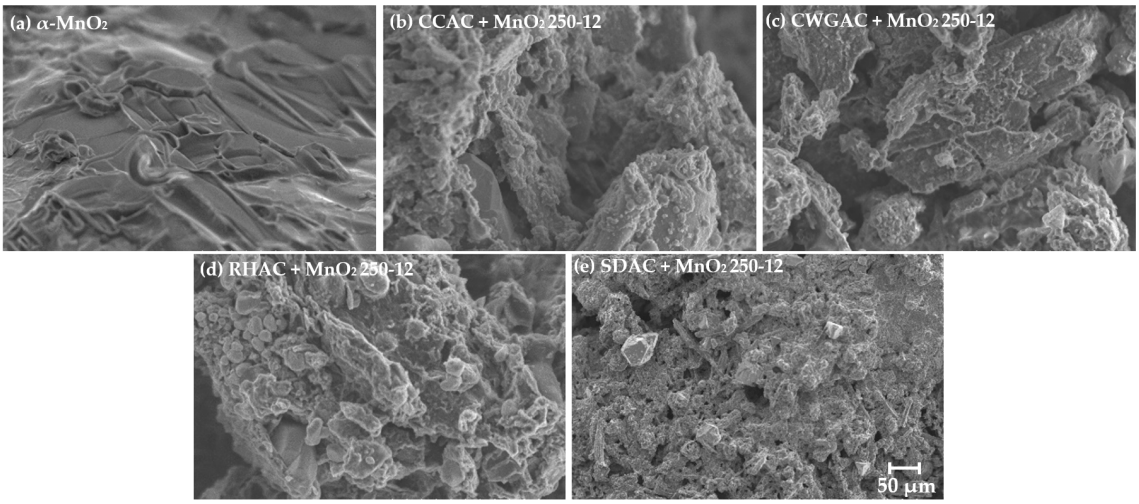

Figure 6. SEM images at 2500× magnification for (**a**) α–MnO_2 and after embedding MnO_2 to activated hydrochar (**b**) CCAC + MnO_2, (**c**) CWGAC + MnO_2, (**d**) RHAC + MnO_2 and (**e**) SDAC + MnO_2 from HTC at 250 °C at 12 h.

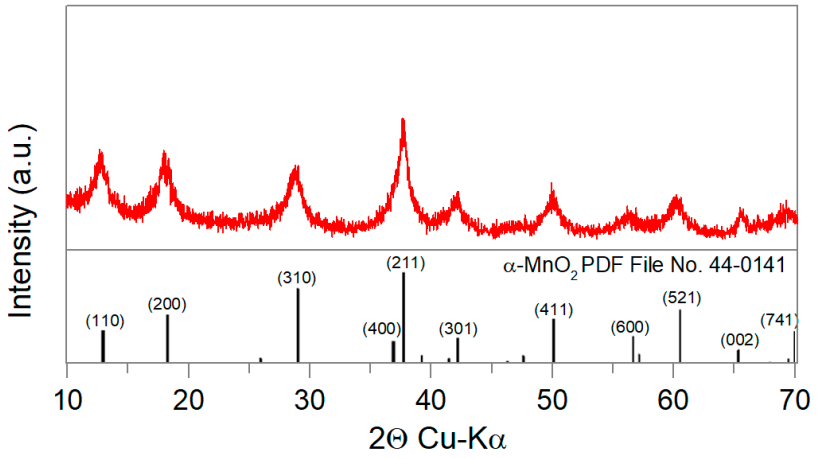

Figure 7. XRD pattern of the synthesized MnO_2.

2.4. ORR Activity

In Figure 8, the cyclic voltammetry (CV) curves of activated carbon (AC) derived from hydrochars with embedded α-MnO_2 were obtained after three cycles from 0.035 to −0.096 V vs. Ag/AgCl at a scan rate of 50 mV s^{-1} in 0.1 M KOH electrolyte saturated with N_2 or O_2. The CV curves in the N_2-saturated solutions showed capacitive behavior in all cases. The appearance of peaks in the O_2-saturated solution is thus attributed to ORR. Well-defined cathodic peaks corresponding to ORR were obtained from CCAC + MnO_2 and CWGAC + MnO_2 in contrast with RHAC + MnO_2 and SDAC + MnO_2. In the same figure, CCAC + MnO_2 250-12 shows the highest area enclosed in the CV curve, which is indicative of the power per active surface area of the electrocatalyst (W cm^{-2}) resulting to a better ORR performance.

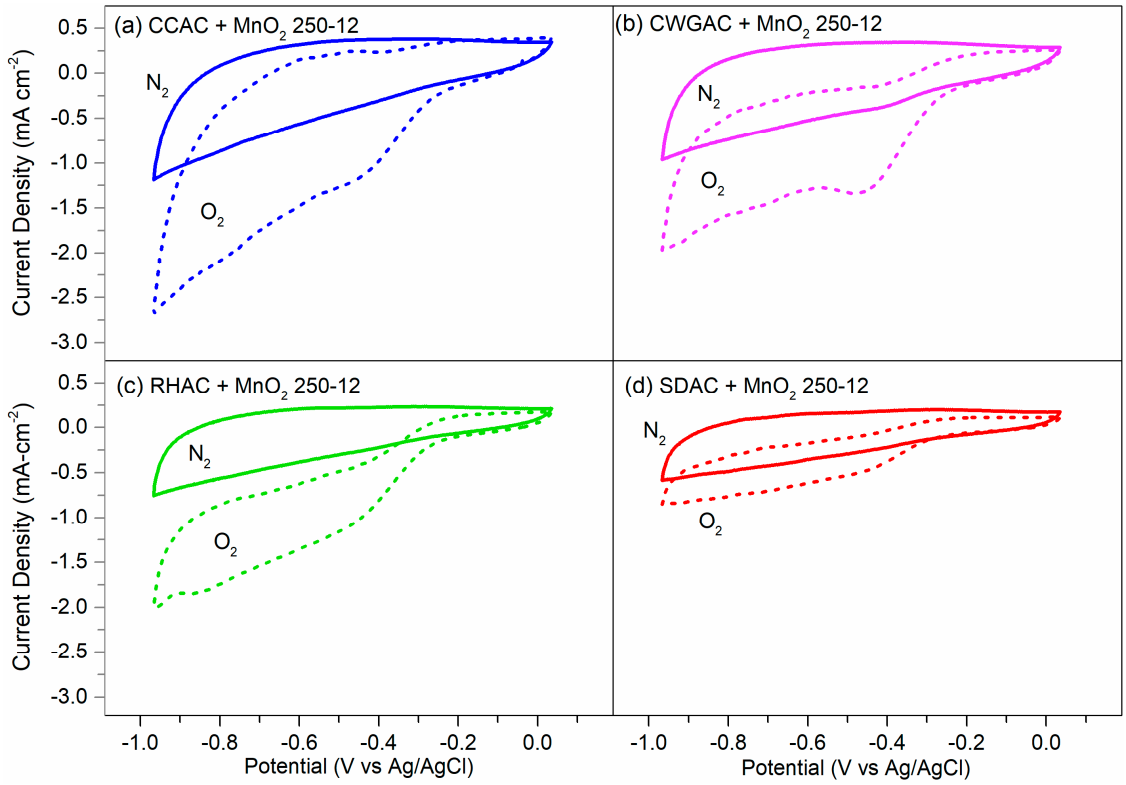

Figure 8. Cyclic voltammetry (CV) results for (**a**) CCAC + MnO_2 250-12, (**b**) CWGAC + MnO_2 250-12, (**c**) RHAC + MnO_2 250-12 and (**d**) SDAC + MnO_2 250-12 in N_2 and O_2 saturated 0.1 M KOH electrolyte.

The ORR performance of pure AC were then compared using linear sweep voltammetry (LSV) along with hydrochars and AC embedded with α-MnO_2 (Figure 9). LSV was carried out at 1600 rpm in 0.1 M KOH solution. The results show that the activation process consistently improved the ORR performance of their unactivated counterparts. The activation process could have potentially increased the open edge sites and curvatures, which assisted oxygen molecules to reach active sites for ORR catalysis [42]. Furthermore, the figures also suggest that the incorporation of α-MnO_2 in the activated carbon improved the ORR performance. This is observed also when doped carbon materials were added to the active electrocatalyst in other studies [10,15,18]. Among the samples that were analyzed, hydrochar and activated carbon produced from HTC at 250 °C for 12 h showed the highest performance, which is consistent with the CV results. Increasing the temperature and duration of HTC leads to the formation of micrometric structures [29,35], thereby improving ORR catalytic activity.

The activity of α-MnO_2 supported by biomass-derived carbons were also compared with Vulcan XC-72 (VC) supported α-MnO_2, and 20% Pt/C (Figure 10). Comparison of the limiting current density (j_L), onset potential (E_{ons}), and overpotential of samples are shown in Table 3. Results indicate that among the biomass derived samples, CCAC + MnO_2 250-12 exhibited the highest limiting current density (2.85 mA cm^{-2}) and lowest overpotential (0.50 V) at the onset of ORR. However, the values were still lower compared to VC + MnO_2 and 20% Pt/C. The large difference between the limiting current density of 20% Pt/C with the different carbon-supported α-MnO_2 could be attributed to the loading ratio of α-MnO_2 to the carbon support. In the study, α-MnO_2 was estimated to constitute 33% of the catalyst loading. The synthesis method, however, involved the direct incorporation of the carbon during α-MnO_2 synthesis, which may have resulted in a lower catalyst loading. Investigation of an appropriate α-MnO_2 to carbon ratio should be pursued in future works to optimize the performance of the developed carbon-supported electrocatalyst. Onset potentials of hydrothermally-prepared catalysts follow the behavior of biomass derived carbon for ORR since carbonaceous compounds have inherently low ORR activity in alkaline media [48–50]. However, if carbon is used as a support for

the metal oxide, rather than as a pure electrocatalyst, the conductivity of the composite enhances and facilitates the electron transfer to the electroactive sites of the metal oxide. [51]. The support also provides a conducting network that enables charge transfer on the metal oxide surface during electrochemical reactions such as ORR [52].

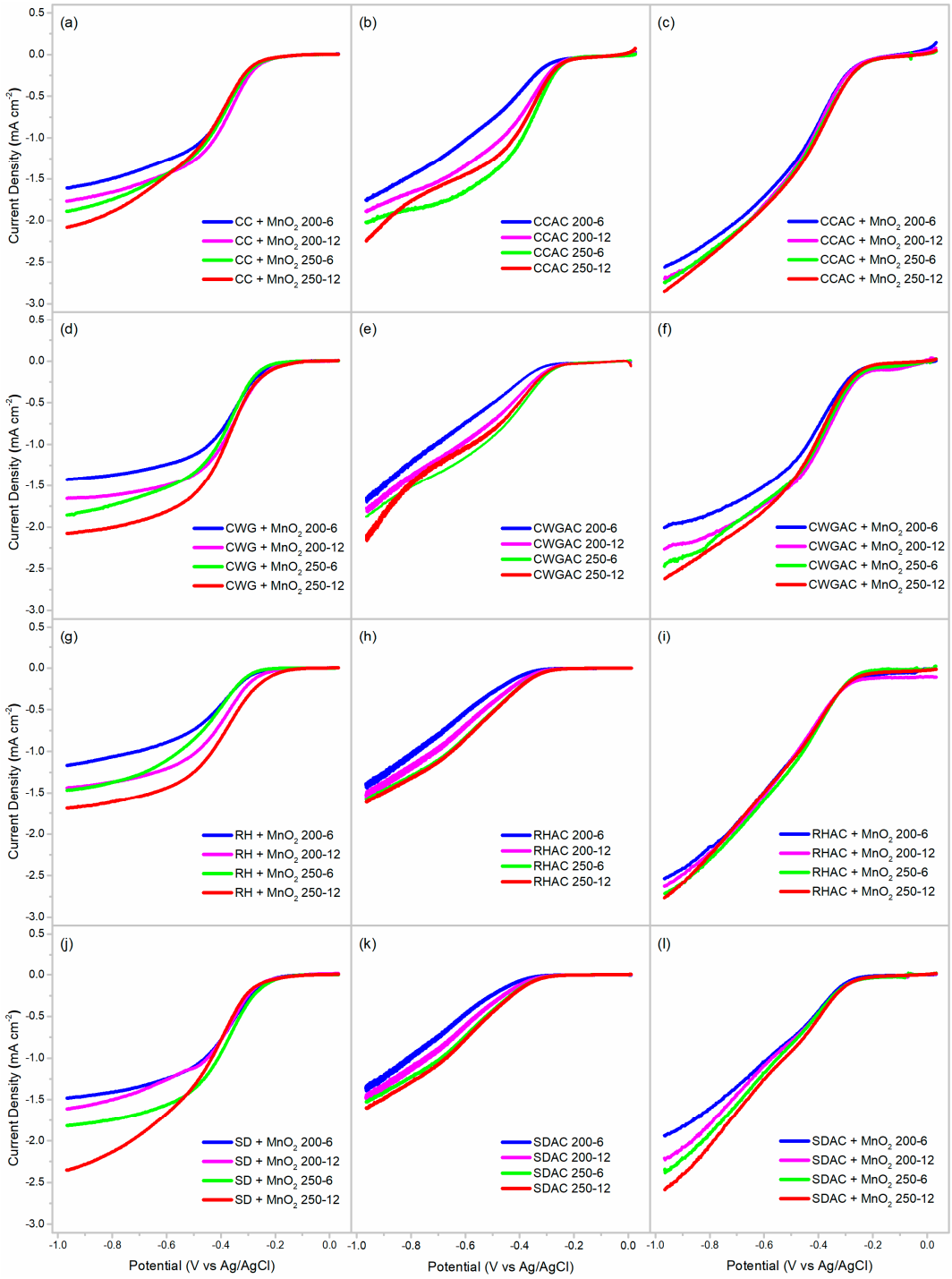

Figure 9. Linear sweep voltammetry (LSV) curves for hydrochar with MnO_2, pure activated carbon (AC) and AC embedded with MnO_2 derived from (**a–c**) corncobs, (**d–f**) coffee waste grounds, (**g–i**) rice hull and (**j–l**) coconut sawdust in 0.1 M KOH at 0.244 mg cm^{-2} loading, scan rate of 5 mV s^{-1} and rotation speed of 1600 rpm.

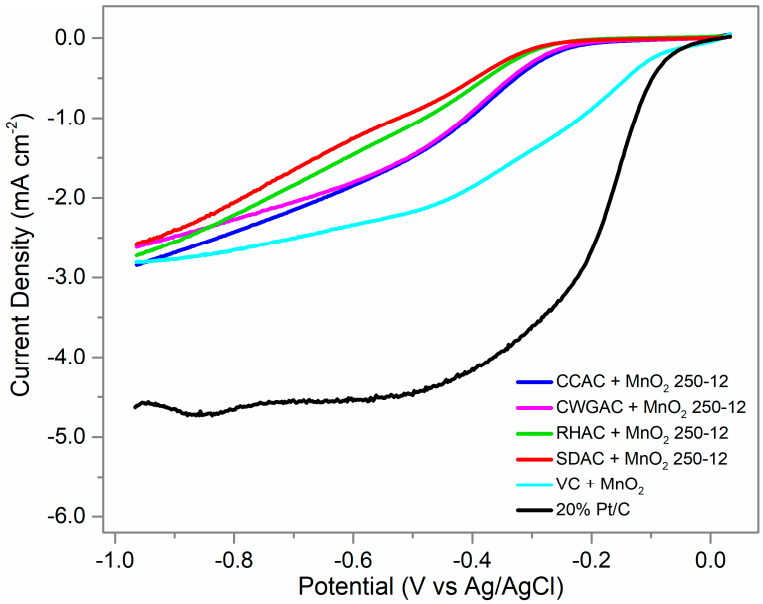

Figure 10. LSV curves for carbon supported MnO_2 of different activated HTC-treated biomass, (Vulcan) supported MnO_2 and 20% Pt/C in 0.1 M KOH at 0.244 mg cm^{-2} loading, scan rate of 5 mV s^{-1} and at 1600 rpm rotation speed.

Table 3. Electrocatalytic activity of carbon supported electrocatalysts and 20% Pt/C.

Sample	j_L (mA cm^{-2})	E_{ons} (V vs. Ag/AgCl)	Overpotential (V)
CCAC + MnO_2 250-12	−2.85	−0.23 (0.73) [1]	0.50
CWGAC + MnO_2 250-12	−2.62	−0.25 (0.71) [1]	0.52
RHAC + MnO_2 250-12	−2.72	−0.35 (0.61) [1]	0.62
SDAC + MnO_2 250-12	−2.58	−0.36 (0.6) [1]	0.63
VC + MnO_2	−2.67	−0.17 (0.79) [1]	0.44
20% Pt/C	−4.63	−0.098 (0.87) [1]	0.36

[1] () V vs. RHE.

The higher performance of the support from corncobs compared to the other biomass can be attributed to the structures left after HTC and KOH activation as discussed in the FTIR results. The regions 1600–1000 cm^{-1} wherein peaks still remain for CCAC 250-12 while others have been greatly reduced, are regions with oxygen-containing functional groups. These functional groups include C=O [34], aryl–O, and C–O [36]. The presence of oxygen-containing groups were found to improve ORR activity in an alkaline environment [53]. It was postulated that the oxygen adsorbed to the active carbon site has a synergistic effect on the oxygen of the carboxyl group. As a result, the carbon to oxygen bond cleaves more easily which benefits the ORR performance [53]. The FTIR results for SDAC 250-12 from Table 2 also indicated the presence of the said functional groups. However, its low activity can be attributed to insufficient development of a porous structure, which hindered the progress of electrochemical reactions on the catalyst surface. In addition, CCAC showed the highest carbon concentration in the EDX analysis which can allow for a greater area for the electrocatalyst. Therefore, it is important to consider both the functional groups and the pore structure resulting from HTC and activation to produce the most suitable carbon support.

To further elucidate the electrochemical properties of activated-carbon-supported MnO_2 samples, the electron transfer number was determined through LSV at different rotation speeds (Figure 11). Koutecky–Levich (KL) plots were then generated from −0.96 to −0.75 V vs. Ag/AgCl (Figure 12). The results showed that carbon supported MnO_2 generally follow a 4-e$^-$ pathway for CCAC + MnO_2 250-12 and CWGAC + MnO_2 250-12. On the other hand, RHAC + MnO_2 and SDAC + MnO_2 250-12

showed a combination of a 2-e$^-$ and 4-e$^-$ pathway. The number of electrons transferred is greatest in CCAC + MnO_2 250-12 (Figure 12a) among tested samples, which further supports that carbon support derived from CC has also better ORR performance.

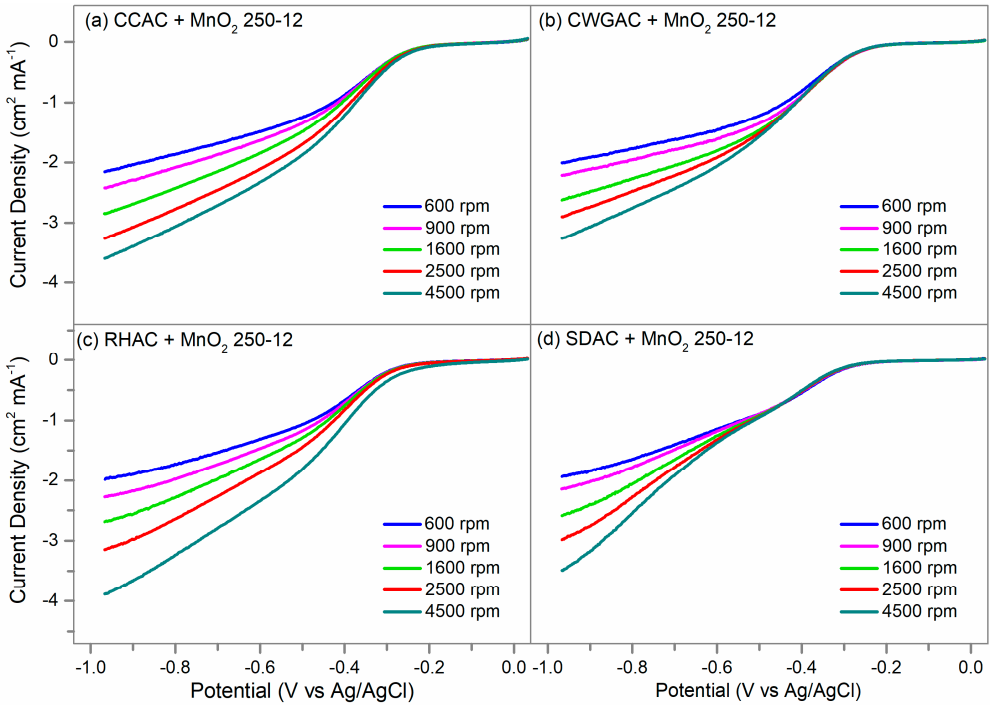

Figure 11. LSV curves for different rotation speeds for (**a**) CCAC + MnO_2 250-12, (**b**) CWGAC + MnO_2 250-12, (**c**) RHAC + MnO_2 250-12 and (**d**) SDAC + MnO_2 250-12.

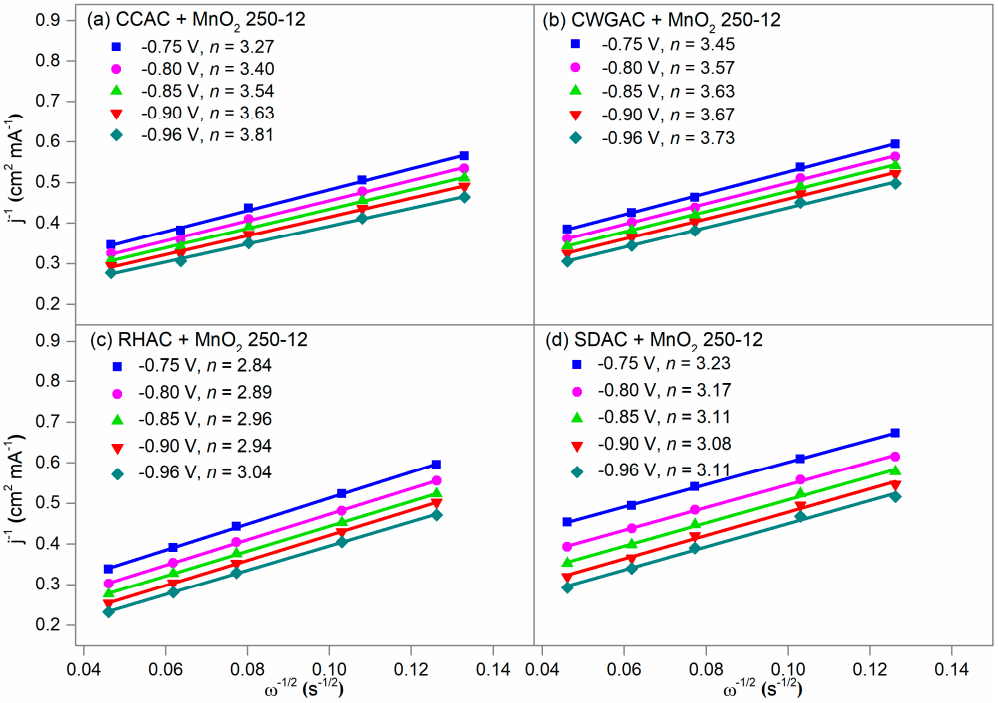

Figure 12. Koutecky–Levich (KL) plots at different potential for (**a**) CCAC + MnO_2 250-12, (**b**) CWGAC + MnO_2 250-12, (**c**) RHAC + MnO_2 250-12 and (**d**) SDAC + MnO_2 250-12.

The ORR mechanism for the electron pathway that an electrocatalyst follows depends on the interaction of oxygen molecules with the catalyst surface. Adsorption of O_2 through a horizontal mode on α-MnO_2 proceeds *via* a bridge-type connection, which is consistent with the 4-e^- pathway [54,55]. While, a vertical mode adsorption follows a two electron 2-e^- reduction pathway [55,56]. Most carbonaceous materials follow a 2-e^- pathway [57] while MnO_2 follows a 4-e^- in an alkaline environment [12,51]. Although the synthesized supports are essentially carbonaceous in nature, differences in the structure of each biomass potentially resulted in different adsorption mechanisms. This implies that CCAC and CWGAC have structures, which supports the electrocatalytic activity of α-MnO_2 towards a horizontal mode of O_2 adsorption and thus favoring the 4-e^- pathway. On the other hand, it can be concluded that RHAC- and SDAC-supported α-MnO_2 exhibits ORR that proceeds both in 2-e^- and 4-e^- pathways, which resulted in an electron transfer number approaching three (3). In other studies [10,19,58], the electron pathway is influenced both by the individual ORR mechanism of the carbon support and the electrocatalyst. For such materials, ORR proceeds both in the composites, hence a mixed behavior can be expected. In this work, the α-MnO_2-mediated pathway for ORR provided a greater contribution compared to the carbon-mediated pathway for CCAC + MnO_2 250-12 and CWGAC + MnO_2 250-12. Whereas, ORR in RHAC + MnO_2 250-12 and SDAC + MnO_2 250-12 proceeded to undergo ORR equally in the carbon support and in α-MnO_2. Therefore, the carbon from CC and CWG were more effective supports for enhancing ORR acitivity of α-MnO_2 compared to those derived from RH and SD since the former group were able to retain the activity of the electrocatalyst.

Material stability is also a concern for carbonaceous compounds and noble metals in ORR electrocatalysis. Accelerated durability tests (ADT) were conducted for CCAC + MnO_2 250-12, VC + MnO_2 and 20% Pt/C in 0.1 M KOH at 50 mV s^{-1} for 5000 cycles. A comparison of limiting current density (j_L) and half wave potential ($E_{1/2}$) is summarized in Table 4 while the voltammetric curves are illustrated in Figure 13. Figure 13e,f show significant reduction of performance for 20% Pt/C. On the other hand, CCAC-MnO_2 250-12 showed less reduction in activity compared to VC + MnO_2. The $E_{1/2}$ for 20% Pt/C showed no changes while significant reduction was observed for VC + MnO_2. A reduction of the limiting current density value was significant for both 20% Pt/C and VC + MnO_2 which amounts to 140% and 98% reduction, respectively. The activity decrease implies the degradation of surface-active sites over time. Meanwhile, CCAC + MnO_2 250-12 showed minor changes in activity compared to the 20% Pt/C and VC + MnO_2, which suggests higher durability.

Table 4. Electrocatalytic properties of catalysts during accelerated durability tests (ADT).

Sample	$E_{1/2}$ (V vs. Ag/AgCl)		j_L (mA cm^{-2})	
	Initial	Final	Initial	Final
CCAC + MnO_2 250-12	−0.32	−0.39	2.85	2.62
VC + MnO_2	−0.29	−0.38	2.67	1.84
20% Pt/C	−0.11	−0.11	4.63	3.79

In this work, we developed a new facile method for the conversion of waste biomass to carbon-based supports for ORR electrocatalysts. The MnO_2-embedded carbon-based catalysts were also successfully synthesized, and their ORR performance analyzed. The use of the carbon-supported MnO_2 catalysts developed in this study could be further tested for metal-air battery systems, which have promising applications as compact power sources and energy storage devices [59]. Successful commercialization has already been reported for primary MABs particularly in zinc-air battery systems [60]. Still, different studies have been made and are still ongoing to address constraints arising from high material costs, low catalytic efficiencies, and poor durability of materials [4–6,18–20]. The catalysts developed in this work are cheap and active alternative cathode materials that can potentially improve the performance of primary MABs. As such, future works are intended to explore the characteristics of the developed electrocatalysts for metal-air battery applications.

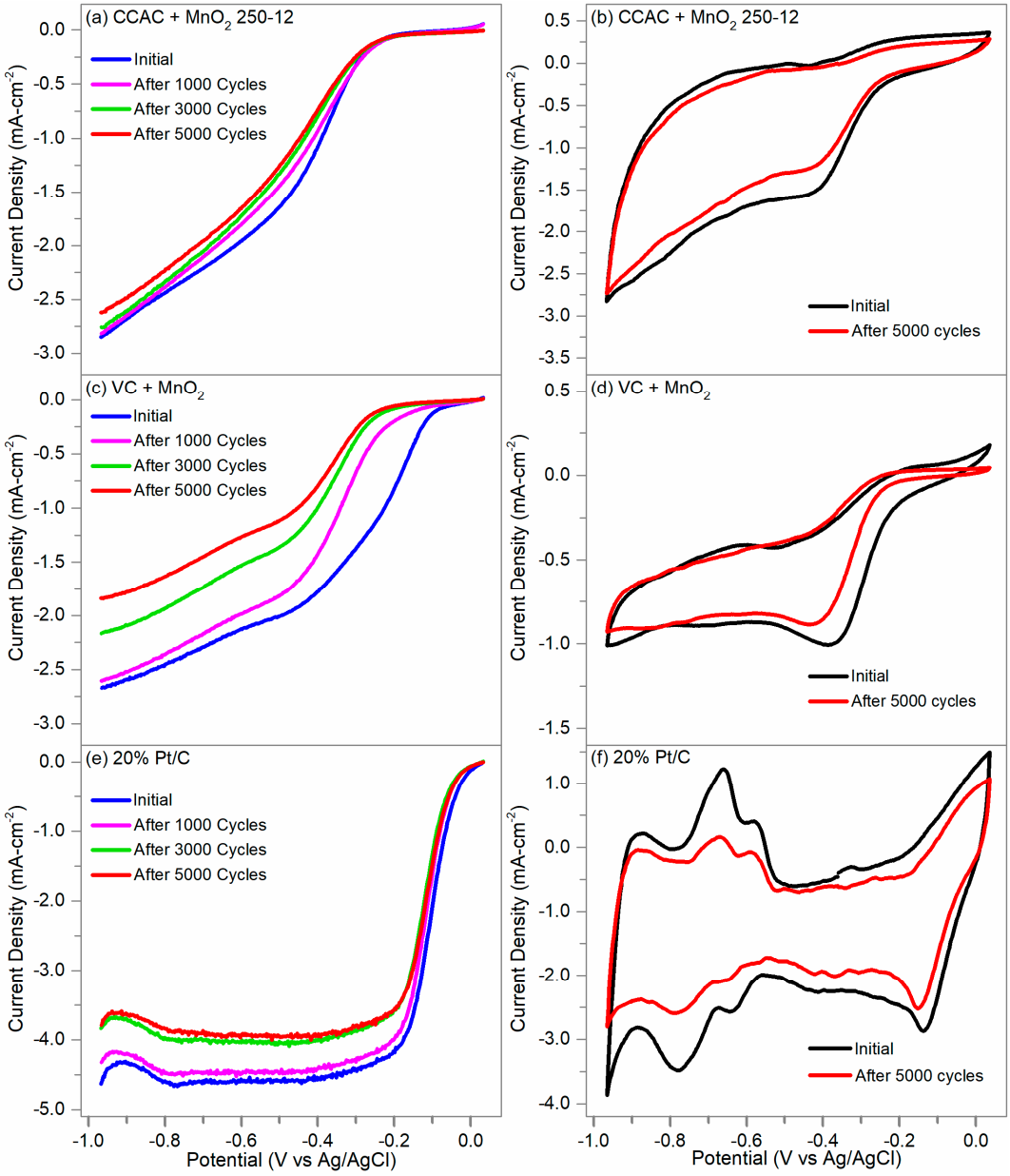

Figure 13. LSV and CV curves for (**a**,**b**) CCAC + MnO_2 250-12, (**c**,**d**) VC + MnO_2 and (**e**,**f**) 20% Pt/C at 0.244 mg cm^{-2} in 0.1 M KOH.

3. Materials and Methods

3.1. Hydrothermal Carbonization

Coffee waste grounds (CWG) were prepared by boiling at 100 °C using deionized water for three hours to remove volatile organic compounds. Corncobs (CC) were first milled into 1 mm product while rice hull (RH) and coconut sawdust (SD) were directly subjected to hydrothermal carbonization (HTC). A ratio of 32 g biomass to 100 mL deionized water was placed in a polytetrafluoroethylene (PTFE)-lined stainless-steel autoclave and was treated in a furnace. Residence time was varied at 6 and 12 h while temperatures were varied at 200 and 250 °C. The hydrochar produced was recovered using filtration and dried in a vacuum oven at 80 °C for 8 h. Samples were then cooled down to room temperature.

3.2. Activation

Hydrochar samples were mixed at a 1:3 ratio with KOH solution (RCI Labscan Ltd., Bangkok, Thailand) and heated to 90 °C for 30 minutes with constant stirring. KOH treated samples were then filtered and dried in a vacuum oven at 90 °C for 4 h. Dried samples were then heat treated in a tube furnace (LTF 12, Lenton Furnaces & Ovens, Hope Valley, United Kingdom) at 600 °C for one hour under N_2 atmosphere (200–300 mL min^{-1}) with a ramp rate of 5 °C min^{-1}. After cooling, the samples were washed with 1 M HCl (RCI Labscan Ltd., Bangkok, Thailand) followed by copious amounts of deionized water. Finally, the activated samples were dried at 90 °C for 4 h in a vacuum oven.

3.3. Incorporation of MnO_2

Equal amounts of 2 M manganese sulfate ($MnSO_4$; Loba Chemie Pvte. Ltd., Mumbai, India) and 2 M ammonium persulfate $(NH_4)_2S_2O_8$ (Loba Chemie Pvte. Ltd., Mumbai, India) were added to activated and hydrochar samples corresponding to the 1:2 *w*/*w* ratio of MnO_2 to carbon. The solution was then transferred to a PTFE lined stainless steel autoclave and hydrothermally treated for 3 h at 120 °C [13]. Samples were then taken out of the autoclave and allowed to cool to room temperature. Finally, the MnO_2 samples were filtered and dried for 6 h in a vacuum oven at 90 °C.

3.4. Material Characterization

Morphological analysis was performed using scanning electron microscopy (SEM; ZEISS Gemini SEM 500, Jena, Germany), determination of crystalline structures using X-ray diffraction (XRD; Maxima XRD-7000 Shimadzu Corporation, Kyoto, Japan), identification of functional groups on the samples surface using Fourier transform infrared (FT-IR) spectroscopy (Nicolet 6700, Wisconsin, USA) and elemental analysis using energy dispersive X-ray spectroscopy (EDX; Phenom XL SEM-EDX, Phenom-World B.V., Eindhoven, Netherlands).

3.5. Electrochemical Measurements

Electrocatalytic activity was measured against a platinum on carbon standard using linear sweep voltammetry (LSV). Samples from hydrochar, and unactivated and activated hydrochar embedded with MnO_2 were analyzed for the difference in electrocatalytic activities. The catalyst ink was prepared by dispersing 6 mg of samples in 950 µL ethanol (RCI Labscan Ltd., Bangkok, Thailand), which was then subjected to ultrasonication for 30 minutes. Then, 50 µL of Nafion solution (5 wt%) (Fuel Cell Store, Texas, USA) was added into the dispersion and ultrasonicated for 20 minutes. Vulcan XC-72 (Fuel Cell Store, Texas, USA) and 20% Pt/C (HiSPEC 3000, John Matthey Fuel Cells, Fuel Cell Store, Texas, USA) catalyst ink were also prepared to serve as standards for ORR performance. Finally, 0.244 mg cm^{-2} loading of the catalysts was dropped in a glassy carbon electron then onto a rotating ring disk electrode (RRDE). Electrochemical measurements were performed using a potentiostat (PGSTAT204, Metrohm, Herisau, Switzerland). The set-up used for voltammetry consisted of RRDE working electrode, Ag/AgCl reference electrode, and a platinum sheet counter electrode. Cyclic voltammetry was performed under N_2- and O_2-saturated 0.1 M KOH solutions at 50 mV s^{-1}. Linear sweep voltammetry was performed at 5 mV s^{-1} scan rate from 0.035 to −0.96 V vs. Ag/AgCl at 1600 rpm.

The number of electrons transferred (*n*) was estimated according to the Koutecky–Levich equation [60].

$$\frac{1}{j} = \frac{1}{B}\omega^{-\frac{1}{2}} + \frac{1}{j_k} \quad (1)$$

$$B = 0.62nFC_o{D_o}^{\frac{2}{3}}v^{-\frac{1}{6}} \quad (2)$$

where *j* is the recorded current density, j_K is the kinetic current density, *w* is the electrode rotating rates (rad s^{-1}), n means the transferred electron number, and *F* is the Faraday constant (96,485 C mol^{-1}).

C_0 (1.2×10^{-3} mol L^{-1}) is the bulk concentration, and D_0 (1.9×10^{-5} cm^2 s^{-1}) corresponds to the diffusion coefficient of O_2 in 0.1 mol L^{-1}. The v represents the kinematic viscosity of the electrolyte (0.01 cm^2 s^{-1}) [61–63].

Accelerated degradation test was then performed from −0.36 to 0.035 V vs. Ag/AgCl at 0.1 M KOH for 5000 cycles. Changes in LSV and CV data were obtained from 0.035 to −0.96 V vs. Ag/AgCl for 1000, 3000 and 5000 cycles.

4. Conclusions

In this work, we successfully synthesized and evaluated carbon support for α-MnO_2 through hydrothermal carbonization followed by KOH activation and heat treatment. High temperature (250 °C) and longer duration (12 h) provided biomass-derived carbon support with better ORR performance due to the formation of pores and micrometric fragments, and the preservation of the lignin backbone structure, which enhances the contact of oxygen to active sites of MnO_2. Further, it was found that activation is a necessary step in the conversion of biomass to carbon support as it functions as the main factor for cellulosic structure degradation and pore formation. Finally, CCAC + MnO_2 250-12 showed the greatest ORR catalytic performance among prepared samples since the conditions were favorable in the formation of porous structures and the preservation of oxygen containing functional group, which facilitated ORR performance. The CCAC + MnO_2 250-12 also showed higher stability compared to VC + MnO_2 and 20% Pt/C. This work provides a new and cost-effective method of deriving carbon support from biomass for enhanced electrocatalytic activity towards ORR. In addition, this synthesized carbon-supported electrocatalyst is seen as a potential cathode for fuel cells and metal-air battery application.

Author Contributions: H.O.P., J.D.A.P. and E.A.E.J. conceived, designed, and performed the synthesis experiments. H.O.P. and J.D.A.P. performed the electroanalytical experiments; J.D.A.P. and E.A.E.J. assisted in project administration; J.A.D.d.R. performed validation of results; H.O.P. prepared the draft manuscript; E.A.E.J., J.A.D.d.R. and J.D.O. reviewed and edited the draft manuscript; J.D.O. provided the overall supervision of the project. All authors have read and agreed to the published version of the manuscript.

Funding: This work is funded by the University of the Philippines Emerging Interdisciplinary Research Program through the Office of the Vice President for Academic Affairs (UP EIDR C08-003). Panganoron would like to thank the Engineering Research and Development for Technology (ERDT) Program of the Department of Science and Technology—Science Education Institute (DOST-SEI) of the Philippines for the graduate scholarship and financial support.

Conflicts of Interest: The authors declare no conflict of interest.

References

1. Davari, E.; Ivey, D.G. Bifunctional electrocatalysts for Zn–air batteries. *Sustain. Energ. Fuels* **2018**, *2*, 39–67. [CrossRef]
2. Pan, H.; Shao, Y.; Yan, P.; Cheng, Y.; Han, K.S.; Nie, Z.; Wang, C.; Yang, J.; Li, X.; Bhattacharya, P.; et al. Reversible aqueous zinc/manganese oxide energy storage from conversion reactions. *Nat. Energy* **2016**, *1*, 2058–7546. [CrossRef]
3. Liu, S.; Han, W.; Cui, B.; Liu, X.; Sun, H.; Zhang, J.; Lefler, M.; Licht, S. Rechargeable zinc air batteries and highly improved performance through potassium hydroxide addition to the molten carbonate eutectic electrolyte. *J. Electrochem. Soc.* **2018**, *165*, A149–A154. [CrossRef]
4. Greeley, J.; Stephens, I.E.L.; Bondarenko, A.S.; Johansson, T.P.; Hansen, H.A.; Jaramillo, T.F.; Rossmeisl, J.; Chorkendorff, I.; Nørskov, J.K. Alloys of platinum and early transition metals as oxygen reduction electrocatalysts. *Nat. Chem.* **2009**, *1*, 552–556. [CrossRef]
5. Osgood, H.; Devaguptapu, S.V.; Xu, H.; Cho, J.P.; Wu, G. Transition metal (Fe, Co, Ni and Mn) oxides for oxygen reduction and evolution bifunctional catalysts in alkaline media. *Nano. Today* **2016**, *11*, 601–625. [CrossRef]
6. Hu, C.; Dai, L. Carbon-based metal-free catalysts for electrocatalysis beyond the ORR. *Angew. Chem. Int. Ed.* **2016**, *55*, 11736–11758. [CrossRef]

7. Wang, Z.; Xu, D.; Xu, J.; Zhang, X. Oxygen electrocatalysts in metal–air batteries: From aqueous to nonaqueous electrolytes. *Chem. Soc. Rev.* **2014**, *43*, 7746–7786. [CrossRef]
8. Li, L. Anchoring Mn_3O_4 nanoparticles on oxygen functionalized carbon nanotubes as bifunctional catalyst for rechargeable zinc-Air battery. *Acs Appl. Energy Mater.* **2018**, *1*, 963–969. [CrossRef]
9. He, Q.; Li, Q.; Khene, S.; Ren, X.; Lopez-Suarez, F.E.; Lozano-Castello, D.; Bueno-Lopez, A. high-loading cobalt oxide coupled with nitrogen-doped graphene for oxygen reduction in anion-exchange-membrane alkaline fuel cells. *J. Phys. Chem. C* **2013**, *117*, 8697–8707. [CrossRef]
10. Wang, M.; Chen, K.; Liu, J.; He, Q.; Li, G.; Li, F. Efficiently enhancing electrocatalytic activity of α-MnO_2 nanorods/N-doped ketjenblack carbon for oxygen reduction reaction and oxygen evolution reaction using facile regulated hydrothermal treatment. *Catalysts* **2018**, *8*, 138. [CrossRef]
11. Cheng, F.; Su, Y.; Liang, J.; Tao, Z.; Chen, J. MnO_2-based nanostructures as catalysts for electrochemical oxygen reduction in alkaline media. *Chem. Mater.* **2010**, *22*, 898–905. [CrossRef]
12. Lima, F.H.B.; Calegaro, M.L.; Ticianelli, E.A. Electrocatalytic activity of manganese oxides prepared by thermal decomposition for oxygen reduction. *Electrochim. Acta* **2007**, *52*, 3732–3738. [CrossRef]
13. Moon, J.; Munakata, H.; Kajihara, K.; Nakamura, K. Hydrothermal synthesis of manganese dioxide nanoparticles as cathode material for rechargeable batteries. *Electrochemistry* **2013**, *81*, 2–6. [CrossRef]
14. Valim, R.B.; Santos, C.M.; Lanza, M.; Machado, S.A.; Lima, F.H.B.; Calegaro, M. Oxygen reduction reaction catalyzed by ε-MnO_2: Influence of the crystalline structure on the reaction mechanism. *Electrochim. Acta* **2012**, *85*, 423–431. [CrossRef]
15. Xu, N.; Nie, Q.; Luo, L.; Yao, C.Z.; Gong, Q.; Liu, Y.; Zhou, X.; Qiao, J. Controllable hortensia-like MnO_2 synergized with carbon nanotubes as an efficient electrocatalyst for long-term metal–air batteries. *Acs Appl. Mater. Interfaces* **2018**, *11*, 578–587. [CrossRef]
16. Smith, M.W.; Shekhawat, D. Fuel Cells: Technologies for Fuel Processing. In *Chapter 5—Catalytic Partial Oxidation*; Shekhawat, D., Spivey, J.J., Berry, D.A., Eds.; Elsevier: Amsterdam, The Netherlands, 2011; pp. 73–128. [CrossRef]
17. Wei, Q.; Fu, Y.; Zhang, G.; Sun, S. Rational design of carbon-based oxygen electrocatalysts for zinc–air batteries. *Curr. Opin. Electrochem.* **2017**, *4*, 45–59. [CrossRef]
18. Fu, G.; Tang, Y.; Lee, J.M. Recent advances in carbon-based bifunctional oxygen electrocatalysts for Zn−air batteries. *ChemElectroChem* **2018**, *5*, 1424–1434. [CrossRef]
19. Kasturi, P.R.; Araunchander, A.; Kalpana, D.; Selvan, R.K. Bio-derived carbon as an efficient supporting electrocatalyst for the oxygen reduction reaction. *J. Phys. Chem. Solids* **2019**, *124*, 305–311. [CrossRef]
20. Gao, Z.; Zhang, Y.; Song, N.; Li, X. Biomass-derived renewable carbon materials for electrochemical energy storage. *Mater. Res. Lett* **2017**, *5*, 69–88. [CrossRef]
21. Ioannidou, O.; Zabaniotou, A. Agricultural residues as precursors for activated carbon production – A review. *Renew. Sustain. Energy Rev.* **2007**, *11*, 1966–2005. [CrossRef]
22. Wu, H.; Geng, J.; Ge, H.; Guo, Z.; Wang, Y.; Zheng, G. Egg-derived mesoporous carbon microspheres as bifunctional oxygen evolution and oxygen reduction electrocatalysts. *Adv. Energy Mater.* **2016**, *6*, 1600794. [CrossRef]
23. Li, B.; Geng, D.; Lee, S.; Ge, X.; Chai, J.; Wang, Z.; Zhang, J.; Liu, Z.; Hor, T.; Zong, Y. Eggplant-derived microporous carbon sheets: Towards mass production of efficient bifunctional oxygen electrocatalyst at low cost for rechargeable Zn-Air Batteries. *ChemComm* **2015**, *51*, 8841–8844. [CrossRef] [PubMed]
24. Wan, W.; Wang, Q.; Zhang, L.; Liang, H.W.; Chen, P.; Yu, S.H. N-, P-and Fe-tridoped nanoporous carbon derived from plant biomass: An excellent oxygen reduction electrocatalyst for zinc–air batteries. *J. Mater. Chem. A* **2016**, *4*, 8602–8609. [CrossRef]
25. Wang, T.; Zhai, Y.; Zhu, Y.; Li, C.; Zeng, G. A review of the hydrothermal carbonization of biomass waste for hydrochar formation: Process conditions, fundamentals, and physicochemical properties. *Renew. Sustain. Energy Rev.* **2018**, *90*, 223–247. [CrossRef]
26. Zhao, P.; Shen, Y.; Ge, S.; Yoshikawa, K. Energy recycling from sewage sludge by producing solid biofuel with hydrothermal carbonization. *Energy Convers Manag* **2014**, *78*, 815–821. [CrossRef]
27. Knez, Ž.; Markočič, E.; Hrnčič, M.K.; Ravber, M.; Škerget, M. High pressure water reforming of biomass for energy and chemicals: A short review. *J. Supercrit Fluids* **2015**, *96*, 46–52. [CrossRef]
28. Funke, A.; Ziegler, F. Hydrothermal carbonization of biomass: A summary and discussion of chemical mechanisms for process engineering. *Biofuels. Bioprod. Bioref.* **2010**, *4*, 160–177. [CrossRef]

29. Xu, Q.; Qian, Q.; Quek, A.; Ai, N.; Zeng, G.; Wang, J. Hydrothermal carbonization of macroalgae and the effects of experimental parameters on the properties of hydrochars. *Acs Sustain. Chem. Eng.* **2013**, *1*, 1092–1101. [CrossRef]
30. Zhang, L.; Liu, S.; Wang, B.; Wang, Q.; Yang, G.; Chen, J. Effect of residence time on hydrothermal carbonization of corn cob residual. *BioResources* **2015**, *10*, 3979–3986. [CrossRef]
31. Sumtong, P.; Chollacoop, N.; Eiad-ua, A. Effect of temperature and times by hydrothermal carbonization process from sawdust and bagasse for carbon materials supporter. *J. Appl. Sci.* **2017**, *16*, 93–97. [CrossRef]
32. Hoffmann, V.; Jung, D.; Zimmermann, J.; Rodriguez Correa, C.; Elleuch, A.; Halouani, K.; Kruse, A. Conductive carbon materials from the hydrothermal carbonization of vineyard residues for the application in electrochemical double-layer capacitors (EDLCs) and direct carbon fuel cells (DCFCs). *Materials* **2019**, *12*, 1703. [CrossRef] [PubMed]
33. Song, M.; Jin, B.; Xiao, R.; Yang, L.; Wu, Y.; Zhong, Z.; Huang, Y. The comparison of two activation techniques to prepare activated carbon from corn cob. *Biomass Bioenerg* **2013**, *48*, 250–256. [CrossRef]
34. Zhang, X.; Zhang, L.; Li, A. Hydrothermal co-carbonization of sewage sludge with pinewood sawdust for nutrient-rich hydrochar production: Synergistic effects and products characterization. *J. Environ. Manag.* **2017**, *201*, 52–62. [CrossRef]
35. Zbair, M.; Bottlinger, M.; Ainassaari, K.; Ojala, S.; Stein, O.; Keiski, R.; Bensitel, M.; Brahmi, R. Hydrothermal carbonization of argan nut shell: Functional mesoporous carbon with excellent performance in the adsorption of Bisphenol A and Diuron. *Waste Biomass Valori* **2018**, 1–20. [CrossRef]
36. Reza, M.T.; Wirth, B.; Lüder, U.; Werner, M. Behavior of selected hydrolyzed products during hydrothermal carbonization of biomass. *Bioresour. Technol.* **2014**, *169*, 352–361. [CrossRef]
37. Khataee, A.; Kayan, B.; Kalderis, D.; Karimi, A.; Akay, S.; Konsolakis, M. Ultrasound-assisted removal of Acid Red 17 using nanosized Fe_3O_4-loaded coffee waste hydrochar. *Ultrason. Sonochem.* **2017**, *35*, 72–80. [CrossRef]
38. Li, X.; Strezov, V.; Kan, T. Energy recovery potential analysis of spent coffee grounds pyrolysis products. *J. Anal. Appl. Pyrolysis* **2014**, *110*, 79–86. [CrossRef]
39. Liu, C.; Huang, X.; Kong, L. Efficient low temperature hydrothermal carbonization of Chinese reed for biochar with high energy density. *Energies* **2017**, *10*, 2094. [CrossRef]
40. Titirici, M.M. Porous Hydrothermal Carbons. In *Sustainable Carbon Materials from Hydrothermal Processes*; Wiley Editors: School of Engineering and Materials Science, Queen Mary, University of London, UK, 2013; pp. 37–73. [CrossRef]
41. Kang, S.; Li, X.; Fan, J.; Chang, J. Characterization of hydrochars produced by hydrothermal carbonization of lignin, cellulose, D-xylose, and wood meal. *Ind. Eng. Chem. Res.* **2012**, *51*, 9023–9031. [CrossRef]
42. Kalderis, D.; Kotti, M.; Méndez, A.; Gascó, G. Characterization of hydrochars produced by hydrothermal carbonization of rice husk. *Solid Earth* **2014**, *6*, 477–483. [CrossRef]
43. Kim, D.; Lee, K.; Bae, D.; Park, K.Y. Characterizations of biochar from hydrothermal carbonization of exhausted coffee residue. *J. Mater. Cycles Waste Manag.* **2017**, *19*, 1036–1043. [CrossRef]
44. Lin, G.; Ma, R.; Zhou, Y.; Liu, Q.; Dong, X. KOH activation of biomass-derived nitrogen-doped carbons for supercapacitor and electrocatalytic oxygen reduction. *Electrochim. Acta* **2017**, *261*, 49–57. [CrossRef]
45. Yun, C.; Park, Y.; Park, C. Effects of pre-carbonization on porosity development of activated carbons from rice straw. *Carbon* **2001**, *39*, 559–567. [CrossRef]
46. Xu, K.; Li, Y.; Xiong, J.; Ou, X.; Su, W.; Zhong, G.; Yang, C. Activated amorphous carbon with high-porosity derived from camellia pollen grains as anode materials for lithium/sodium ion batteries. *Front. Chem.* **2018**, *6*, 366. [CrossRef]
47. Saad, M.J.; Chia, C.; Zakaria, S.; Sajab, M.S.; Misran, S.; Bin Abdul Rahman, M.H.; Chin, S.X. Physical and chemical properties of the rice straw activated carbon produced from carbonization and KOH activation processes. *Sains Malays.* **2019**, *48*, 385–391. [CrossRef]
48. Sidik, R.; Anderson, A.; Subramanian, N.; Kumaraguru, S.; Popov, B. O_2 Reduction on graphite and nitrogen-doped graphite: Experiment and theory. *J. Phys. Chem. B* **2006**, *110*, 1787–1793. [CrossRef]
49. Maldonado, S.; Stevenson, K. Influence of nitrogen doping on oxygen reduction electrocatalysis at carbon nanofiber electrodes. *J. Phys. Chem. B* **2005**, *109*, 4707–4716. [CrossRef]
50. Li, Y.; Dai, H. Recent advances in Zinc-air batteries. *Chem. Soc. Rev.* **2014**, *43*, 5257–5275. [CrossRef]

51. Xu, N.; Qiao, J.; Zhang, X.; Ma, C.; Jian, S.; Liu, Y.; Pei, P. Morphology controlled La2O3/Co3O4/MnO2–CNTs hybrid nanocomposites with durable bi-functional air electrode in high-performance zinc–air energy storage. *Appl. Energy* **2016**, *175*, 495–504. [CrossRef]
52. Basirun, W.J.; Sookhakian, M.; Baradaran, S.; Endut, Z.; Mahmoudian, M.R.; Ebadi, M.; Yousefi, R.; Ghadimi, H.; Ahmad, S. Graphene oxide electrocatalyst on MnO_2 air cathode as an efficient electron pump for enhanced oxygen reduction in alkaline solution. *Sci. Rep.* **2015**, *5*, 1–7. [CrossRef]
53. Zhong, R.S.; Qin, Y.H.; Niu, D.F.; Tian, J.W.; Zhang, X.S.; Zhou, X.G.; Sun, S.G.; Yuan, W.K. Effect of carbon nanofiber surface functional groups on oxygen reduction in alkaline solution. *J. Power Sources* **2013**, *225*, 192–199. [CrossRef]
54. Roche, I.; Chaînet, E.; Chatenet, M.; Vondrák, J. Durability of carbon-supported manganese oxide nanoparticles for the oxygen reduction reaction (ORR) in alkaline medium. *J. Appl. Electrochem.* **2008**, *38*, 1195–1201. [CrossRef]
55. Woon, C.; Islam, A.; Tharan, B.; Ong, H.R.; Cheng, C.K.; Chong, K.F.; Hedge, G.; Khan, M. Carbon nanotube-modified MnO_2: An efficient electrocatalyst for oxygen reduction reaction. *ChemistrySelect* **2017**, *2*, 7637–7644. [CrossRef]
56. Karuppiah, S.; Senthil Kumar, S.M.; Rangasamy, T.; Ganesan, K.; Murugan, P.; Rajput, P.; Jha, S.; Bhattacharyya, D. Physiochemical investigation of shape designed MnO_2 nanostructures and their influence on oxygen reduction reaction activity in alkaline solution. *J. Phys. Chem. C* **2015**, *119*, 6604–6618. [CrossRef]
57. Gu, P.; Zheng, M.; Zhao, Q.; Xiao, X.; Xue, H.; Pang, H. Rechargeable zinc–air batteries: A promising way to green energy. *J. Mater. Chem. A* **2017**, *5*, 7651–7666. [CrossRef]
58. Molina-García, M.; Rees, N. Effect of catalyst carbon supports on the oxygen reduction reaction in alkaline media: A comparative study. *RSC Adv.* **2016**, *6*, 94669–94681. [CrossRef]
59. Yu, Y.; Hu, A. Recent progress of metal-air batteries—a mini review. *Appl. Sci.* **2019**, *9*, 2787. [CrossRef]
60. Clark, S.; Latz, A.; Horstmann, B. A review of model-based design tools for metal-air batteries. *Batteries* **2018**, *4*, 5. [CrossRef]
61. Zhou, R.; Zheng, Y.; Jaroniec, M.S.; Qiao, Z. Determination of the electron transfer number for the oxygen reduction reaction: From theory to experiment. *ACS Catal* **2016**, *6*, 4720–4728. [CrossRef]
62. Wang, G.; Peng, H.; Qiao, X.; Du, L.; Li, X.; Shu, T.; Liao, S. Biomass-derived porous heteroatom-doped carbon spheres as a high-performance catalyst for the oxygen reduction reaction. *Int. J. Hydrog. Energy* **2016**, *41*, 14101–14110. [CrossRef]
63. Li, X.; Xu, N.; Li, H.; Wang, M.; Zhang, L.; Qiao, J. 3D hollow sphere Co_3O_4/MnO_2-CNTs: Its high-performance bi-functional cathode catalysis and application in rechargeable zinc-air battery. *Green Energy Environ.* **2017**, *2*, 316–328. [CrossRef]